To appear in *Atmosphere-Ocean*

Vol. 00, No. 00, Month 20XX, 1–41

Changes in Oceanic Carbon Storage due to Anthropogenic Carbon Input over the Past Three Decades

Fengjue Hong[1] and Varvara E. Zemskova[2*]

[1] *University of Waterloo, Department of Geography and Environmental Management, 200 University Ave W, Waterloo, ON N2L 3G1, Canada;* [2] *University of Waterloo, Department of Applied Mathematics, 200 University Ave W, Waterloo, ON N2L 3G1, Canada*

(Original manuscript received 00 Month 20XX; accepted 00 Month 20XX)

This is a non-peer-reviewed preprint that has been submitted to *Atmosphere-Ocean*.

*Corresponding author's email: barbara.zemskova@uwaterloo.ca

While the ocean is known to be an important sink for anthropogenic CO_2 emissions, assessing trends in ocean's uptake and storage of atmospheric CO_2 is complicated because changes in the ocean dissolved inorganic carbon (DIC) concentrations due to natural ocean circulation patterns and flux of anthropogenic CO_2 need to be disentangled. In this study, we analyze the interannual and decadal changes in the ocean anthropogenic DIC storage from 1992 *to* 2022 *using data from the physically and biogeochemically consistent ECCO-Darwin ocean state estimate model. We use the quasi-conservative tracer C^* to represent the ocean anthropogenic DIC concentrations and offer several key extensions to previous studies: (1) a longer period of analysis (three decades), (2) analysis including the Arctic Ocean, (3) regular spatio-temporal coverage using annually-averaged data to more accurately estimate the rates of change of C^*. Over the* 1992–2022 *period, we estimate a total global ocean C^* increase of 60 Pg C, corresponding to about 28% of total anthropogenic CO2 emissions during this time. The general temporal trend shows a nonlinear increase with accelerating rates of anthropogenic DIC accumulation especially in the last two decades (*$2002 - 2022$*), though a slowdown in the increasing rates is found in some parts of the ocean, in particular in high-nutrient low-chlorophyll regions. Empirical Orthogonal Function analysis of the vertically-integrated rates of change of C^* reveals that the top four modes of interannual variability correspond to the Pacific climate modes, such as El Niño Southern Oscillation, Pacific Decadal Oscillation, and North Pacific Gyre Oscillation.*

KEYWORDS: ocean carbon sink,

1 Introduction

The ocean plays a critical role in the Earth system; it stores, absorbs, releases, and exchanges carbon from the atmosphere. It is the second largest carbon reservoir, which stores approximately 60 times as much carbon as the atmosphere, surpassed only by the solid Earth, mostly in limestone and shale rocks which stores roughly $100,000$ times more carbon than the atmosphere (DeVries, 2022). Since the Industrial Revolution, human activities have led to the continuous emissions of large amounts of carbon dioxide (IPCC, 2023). The large carbon emissions in the atmosphere not only changed the composition of the atmosphere, but also significantly aggravated the instability of the ocean's carbon absorption mechanism (IPCC, 2023). This has led to an imbalance in the carbon cycle that has long maintained the stability of the Earth's climate, such as risk to the ecosystems and threats to human development (Trebilco et al., 2022). Specifi-

cally, the large amount of carbon emissions has triggered a series of environmental crises such as global warming, frequent extreme weather, and rising sea levels (United Nations Development Programme (UNDP), 2023). Low-income regions and island countries on the socioeconomic margins are particularly vulnerable to these changes (Chin-Yee, 2019; Luetz & Merson, 2020). Rising ocean temperatures and acidification affect the stability of fishery ecology and food chains, exacerbating the survival pressure on groups that rely on marine resources for their livelihoods (Trebilco et al., 2022).

Therefore, there is an imminent need to understand the temporal trends in ocean carbon sink to assess the ocean's potential to take up more carbon dioxide from the atmosphere. In response to the increase in atmospheric carbon and changes to the Earth's carbon cycle, numerous studies investigated the ocean carbon flux and the dissolved inorganic carbon (DIC) budget. For example, recent studies on ocean carbon storage at the decadal scales have shown that while from the 1990s to early 2000s, the global ocean carbon sink was decreasing, in the 2000s and 2010s, the ocean carbon sink has strengthened (DeVries, Holzer, & Primeau, 2019; Landschützer et al., 2015; Zemskova, He, Wan, & Grisouard, 2022). However, as ocean DIC measurements are sparse (L. Talley et al., 2016), there have been many different methodologies employed to attempt to capture the spatial and temporal (both short-term such as seasonal cycles, and long-term, such as interannual and decadal scales) patterns.

The DIC budget changes are controlled not only at the ocean surface but also within the ocean interior by several processes: physical processes, biogeochemical processes, thermodynamic effects, and anthropogenic impacts (Carroll et al., 2022; Sarmiento & Gruber, 2006). Physical processes include advection, diffusion and mixing, and air–sea CO_2 flux. Advection is characterized by the large-scale ocean circulation transports water masses with varying DIC concentrations, whereas diffusion and mixing act on small spatiotemporal scales primarily redistributing DIC across depth layers, shaping vertical DIC gradients. Air–sea CO_2 flux is the exchange of CO_2 between sea surface and the atmosphere, which directly affects the surface DIC concentration. Anthropogenic emissions impact increase the total atmospheric CO_2, which gradually enters

the ocean through the air–sea CO_2 flux, causing the rise in surface DIC concentrations over time. Biogeochemical processes include changes to the ocean DIC pool through net community production (i.e., incorporation of DIC into the organic matter pool through photosynthesis) and remineralization (i.e., decomposition of organic matter back into inorganic components). Thermodynamic effects are due to changes in ocean temperature; for example, the increasing temperature in ocean decreases the solubility of CO_2 in seawater, thereby influencing the equilibrium distribution of DIC, especially at the surface. As such, both the natural and anthropogenic processes can change the DIC in the ocean, and it is necessary to separate the effects of the two on the ocean DIC spatio-temporal trends.

Many studies have aimed to monitor the changes in ocean carbon sink by estimating air-sea carbon fluxes at the ocean surface (e.g., Fay & McKinley, 2013; Gregor & Gruber, 2020; Rödenbeck et al., 2015; Rödenbeck, DeVries, Hauck, Le Quéré, & Keeling, 2021). For example, (Landschützer et al., 2015) applied a neural network approach to interpolate the sparse and spatio-temporally heterogeneous observations of surface partial pressure of CO_2 (pCO_2) to study the Southern Ocean carbon sink. (Bushinsky et al., 2019) compared the different interpolation strategies assessing how data from biogeochemical Argo floats can augment shipboard observations, which are in particularly scarce in the winter in the Southern Ocean. In another study, (Mayot et al., 2024) used a hybrid approach combining the physical and biogeochemical coupled model NEMO-PlankTOM12.1 and observed SOCAT fCO_2 (fugacity of carbon dioxide) data at the surface to improve the model estimates, specifically to constrain the trend of the ocean carbon sink from 2000 to 2022. The study showed this method can help minimize the differences between process-based numerical models and observations of estimated global carbon budget over this period.

In recent years, there also have been efforts to understand the variability of DIC within the ocean interior through climatological averages (e.g., Bronselaer et al., 2020; Lauvset et al., 2022), coupled ocean circulation models (e.g., Carroll et al., 2020; Verdy & Mazloff, 2017), and machine-learning methods (e.g., Broullón et al., 2020; Keppler, Landschützer, Gruber, Lauvset,

& Stemmler, 2020; Keppler, Landschützer, Lauvset, & Gruber, 2023; Zemskova et al., 2022). However, in addition to differences, both in total magnitude and regionally, across methods in estimating ocean carbon uptake (DeVries et al., 2023; Gray, 2024), these datasets do not provide the breakdown between the natural and anthropogenic-driven changes in the ocean DIC pool. One of the methods to estimate the natural DIC signal uses the organic matter remineralization stoichiometric ratios relating DIC to either dissolved oxygen concentrations (Gruber, Sarmiento, & Stocker, 1996) or dissolved nitrate, and phoshate concentrations (Gruber & Sarmiento, 2002). This method has been successfully implemented to provide estimates in changes of DIC of natural and anthropogenic origin along certain repeated hydrographic transects (Carter et al., 2019; Sabine et al., 1999; Wanninkhof et al., 2010) and globally (Gruber et al., 2019; Mayot et al., 2024). However, because this methodology relies on the readily available data for other biogeochemical variables (e.g., oxygen, nitrate, or phosphate) in the ocean interior, these studies have only been able to provide estimates for inter-decadal changes in the natural and anthropogenic DIC inventories, which do not account for interannual variability and longer-term climatological cycles such as El Niño Southern Oscillation (ENSO) that have been shown to play an important role in distribution of ocean DIC (Carroll et al., 2022; DeVries et al., 2023; Keppler et al., 2023).

To address this limitation of the previous studies, we apply the methodology of Gruber and Sarmiento (2002) to the output of the ECCO-Darwin model (Carroll et al., 2020), which provides three-dimensional data for biogeochemical variables on regular spatio-temporal intervals, to estimate annual changes in the global ocean storage of anthropogenic DIC over the $1992 - 2022$ period. The ECCO-Darwin model is a global ocean biogeochemistry model that couples the Estimating the Circulation and Climate of the Ocean (ECCO) model for physical processes in the ocean and an ecosystem model developed by the Massachusetts Institute of Technology Darwin Project. One of its major advantages is that it produces continuous, observation-constrained (by data from GLODAPv2 (Lauvset et al., 2022) and other observational databases) outputs for biogeochemical variables (e.g., DIC, nitrate, phosphate, alkalinity, and dissolved oxygen) and physical variables (e.g., temperature, salinity, flow velocity) across seasonal to multidecadal

timescales (Carroll et al., 2020). Because ECCO-Darwin produces three-dimensional fields of the biogeochemical variables on across a set spatial grid at regular temporal intervals with full spatial and temporal coverage regardless of observation density, it allows us to calculate the natural and anthropogenic changes in DIC at every model grid point and at every available timestep. Specifically, in this study, we report annual changes, ignoring smaller scale (e.g., seasonal) variations, on a $1^\circ \times 1^\circ$ horizontal grid from the surface to the ocean bottom to gain a more comprehensive understanding of spatio-temporal trends of the ocean DIC changes decomposed into the natural and anthropogenic components.

We acknowledge that because we are using model-based data as input, our results are subject to any biases that originate from the model configuration, for example, from the parameterization of unresolved small-scale processes or simplification of the biogeochemical cycles. However, with these caveats, this paper provides another set of independent estimates of the natural and anthropogenic ocean DIC changes to better constrain the estimates of ocean carbon storage trends in conjunction with previous studies. Importantly, in their analysis of ocean carbon trends using different available datasets and models for RECCAP2 (REgional Carbon Cycle Assessment and Processes), DeVries et al. (2023) could not quantify the anthropogenic contribution only for the ECCO-Darwin model, as it does not natively provide such breakdown. This study provides such analysis so that it can be considered in future comprehensive assessments.

The manuscript is organized as follows. The overall methodology is presented in § 2 as summarized in § 2.a: method to estimate local anthropogenic portion of DIC in § 2.b, description of the ECCO-Darwin model output used for analysis in § 2.c, and different analysis techniques to assess the spatio-temporal changes in ocean anthropogenic DIC in § 2.d-2.f. The results for temporal trends of changes in anthropogenic carbon in § 3 are presented separately for decadal and annual changes. The decadal trends in § 3.a are integrated vertically and zonally to examine the three-dimensional spatial patterns. For the interannual variability, we examine these spatial patterns in even more detail by splitting the ocean horizontally and vertically into a total of 45 regions (§ 3.b) and through the Empirical Orthogonal Function (EOF) analysis of the

vertically-integrated temporal changes (§ 3.c). The globally-integrated annual changes in ocean anthropogenic carbon concentrations are presented in § 3.d. Finally, we discuss the limitations of this work, in particular due to using modelled data, in § 4 and summarize our main findings and importance of this work in § 5.

2 Data and Methods

2.a *Overview of the Approach*

This study uses the carbon tracer C^* developed by Gruber et al. (1996) as a proxy for anthropogenic carbon, which is one of the standard framework for estimating anthropogenic carbon in the ocean and is described in § 2.b. Unlike the observation-based approach of previous works (Gruber et al., 2019; Müller et al., 2023) that relies on regression-based interpolation of the spatio-temporally sparse cruise data, this study uses monthly data on a regular spatial grid from the ECCO-Darwin model. The specifics of the model are described in § 2.c. The spatio-temporally continuous nature of the data allows us to directly calculate temporal trends of changes in C^* without the need for reference year adjustment unlike these previous studies.

Temporal changes in C^* are calculated over the $1992-2022$ time period. The distribution of C^* is inherently four-dimensional as it is a function of time, latitude, longitude, and depth. We use several analysis methods to reduce this complex problem to two-dimensions that we can plot, which are described in § 2.d. Specifically, we calculate changes in C^* using annually-averaged data (1) on the decadal time scale integrated vertically and zonally, and (2) on the annual time scale integrated globally and over specific ocean regions based on ocean geographic basins and density ranges (defined in § 2.e). We also apply the Empirical Orthogonal Function (EOF) analysis to the monthly-averaged data to study the spatial-temporal patterns of C^* variability and compare it to the known climate variability modes ad described in § 2.f.

2.b C^* *calculation*

As the ocean total DIC is a combination of naturally-produced carbon due to oceanic biogeochemical activity and anthropogenic carbon absorbed from the atmosphere, the method proposed by Gruber et al. (1996) can separate the two by isolating a tracer C^* which represents the anthropogenic carbon. The C^* tracer is computed as:

$$C^* = \mathrm{C} - r_{C:P} \cdot \mathrm{PO_4} - 0.5 \cdot (\mathrm{Alk} + r_{N:P} \cdot \mathrm{PO_4}) \tag{1}$$

where C is the total DIC concentration, and PO_4 (phosphate concentration) and ALK (alkalinity) are used to approximate the natural DIC component based on canonical Redfield stoichiometric ratios, with $r_{C:P} = 117$ and $r_{N:P} = 16$. The resulting residual represents the anthropogenic fraction of DIC, as it cannot be explained by natural biological cycling (Clement & Gruber, 2018). The values for variables of PO_4, ALK and C are retrieved from ECCO-Darwin model output, with a valid period of 1992 to 2022. The Redfield stoichiometric ratios is extracted from Anderson and Sarmiento (1994).

Here, we follow the same assumption as previous studies that estimated changes in ocean anthropogenic DIC (Clement & Gruber, 2018; Gruber et al., 2019; Müller et al., 2023) that the variations in the Redfield ratio are predominantly spatial (Liefer et al., 2024; Martiny et al., 2013; Seelen et al., 2025) and will not affect temporal trends in C^* at any given location. However, it is important to note that recent studies found temporal shifts in stoichiometric ratios to be important (Hutchins & Tagliabue, 2024; Liu et al., 2025), which may need to be incorporated into the calculation of C^* in future studies as an uncertainty parameter. Also, as noted in Clement and Gruber (2018), C^* contains a generally much smaller component of the natural air-sea CO_2 exchange, but predominantly C^* reflects the uptake of anthropogenic CO_2.

2.c *Data Used*

The estimates in this study are based on the data from the ECCO-Darwin model, which is a global ocean biogeochemistry model that combines the global ocean circulation model (physical module) from the Estimating the Circulation and Climate of the Ocean (ECCO) consortium and an ecosystem model (biogeochemical module) developed by the Massachusetts Institute of Technology Darwin Project (Carroll et al., 2020). The ECCO-Darwin ocean state estimate combines a general circulation model with a biogeochemical model through a four-dimensional variational (4D-Var) adjoint assimilation framework (Carroll et al., 2020). In the physical module, the MITgcm ocean circulation model is constrained by a wide range of observational datasets, including satellite altimetry, sea surface temperature, sea ice concentration, and in situ hydrographic profiles from Argo floats, ship-based CTD casts, and moorings. The adjoint method iteratively adjusts model control variables (e.g., surface forcing, initial conditions, and mixing parameters) to minimize the misfit between model output and observations over the full assimilation window. The coupled biogeochemical module (Darwin Project) simulates multiple phytoplankton and zooplankton functional types with variable elemental stoichiometry, allowing for competition and adaptation to changing environmental conditions (Carroll et al., 2020, 2022). The carbon cycle component explicitly represents DIC, alkalinity, nutrients (phosphate, nitrate, silicate), dissolved oxygen, and dissolved organic matter pools (Carroll et al., 2020, 2022). Air–sea CO_2 exchange, remineralization, and biological export production are all resolved within the model framework, providing physically and biogeochemically consistent estimates of the evolving ocean carbon system (Carroll et al., 2020, 2022).

The ECCO-Darwin model is run on a LLC270 (Lat-Lon-Cap 270) grid, which organizes the global ocean into 13 spatial tiles, each with 270×270 horizontal grid points (Carroll et al., 2020). For the ease of visualization, we converted the data onto a regular latitude-longitude grid with 1° horizontal resolution. This resolution was chosen to be consistent with other major ocean biogeochemical datasets, e.g., the World Ocean Atlas (WOA). However, any other horizontal spacing larger than 1/3° degree (the largest horizontal spacing in the native LLC270 grid) could

have been chosen. No masking and further data cleaning was required in this step as the ECCO-Darwin model provides fully gridded and physically consistent data without missing values over the ocean. Data is available at monthly temporal resolution from 1992 to 2022. For different analysis methods, we use both the monthly data (see § 2.f) and annually-averaged data (see § 2.d).

Compared with the real-world observations, the modeled data has a high similarity with observed data in data-rich areas, particularly for temperature, salinity, dissolved oxygen, and alkalinity, as evaluated against datasets such as the World Ocean Atlas (WOA), Argo, and GLODAPv2 (Carroll et al., 2022). For example, in the ECCO-Darwin state estimate, the optimized simulation reduced the total model–data misfit to 31.9% of the first-guess simulation from Brix et al. (2015), with particularly strong improvements for the full-depth three-dimensional variables, e.g., about 95% improvement for DIC and alkalinity. These improvements were evaluated against WOA and Argo observations (Carroll et al., 2020), and, in the extended 1992–2018 version, also against GLODAPv2 biogeochemical data (Carroll et al., 2022). For further details and validations of the model, the readers should refer to Carroll et al. (2020) and Carroll et al. (2022) and the discussion of study limitations in § 4.

2.d *Analysis methodology for temporal trends*

2.d.1 Annual changes

After calculating annually-averaged value of $C^*(x, y, z)$ using Eqn. (1) at each ocean grid cell for latitude x, longitude y, and depth z, we compute the temporal trends of anthropogenic carbon changes in the ocean. The year-to-year changes between year t_2 and year t_1 at each grid point will be denoted as:

$$\Delta C^*(t_2 - t_1, x, y, z) = C^*(t_2, x, y, z) - C^*(t_1, x, y, z). \tag{2}$$

This interannual changes are integrated over 45 different ocean regions in order to examine

the spatial patterns (§ 3.b) and over the whole ocean in order to compare with estimates from other studies and total anthropogenic emissions (§ 3.d). The 45 ocean regions are defined based on the geographic basins (Atlantic, Pacific, Indian, Southern, and Arctic) to divide the global ocean horizontally and neutral density levels to divide the ocean vertically. Further details are provided in § 2.e.

2.d.2 Decadal changes

In addition to the annual changes in C^*, we also compute decadal trends to compare with those based on interpolated observational data presented in previous studies (Gruber et al., 2019; Müller et al., 2023). For our data, to quantify decadal changes in anthropogenic carbon storage, linear regression is applied to the annual $C^*(x, y, z)$ values at each grid cell over selected time periods. The decadal changes over a particular period T are denoted as $\Delta C^*(T, x, y, z)$. We compute decadal changes over three periods: $1993-2002$ (T_1), $2003-2012$ (T_2), and $2013-2022$ (T_3) corresponding to the total span of the ECCO-Darwin model dataset.

Spatial patterns of decadal trends are presented in two ways following Müller et al. (2023). First, in § 3.a.1 we consider vertically-integrated ΔC^* over the entire water column from the local maximum depth to the surface, which we will denote as $\widehat{\Delta C^*}(x, y)$ as a function of latitude x and longitude y. Next, in § 3.a.2 we explore zonally-integrated ΔC^* for each of the five (Atlantic, Pacific, Indian, Southern, and Arctic) ocean basins, denoted as $\widetilde{\Delta C^*}(x, z)$ at each latitude x and depth z.

Furthermore, to provide a more quantitative comparison in the changes in $\widehat{\Delta C^*}$ between decades, we calculate the differences between the decadal trends in C^* as

$$\begin{aligned} \Delta\widehat{\Delta C^*}(T_2 - T_1, x, y) &= \widehat{\Delta C^*}(T_2, x, y) - \widehat{\Delta C^*}(T_1, x, y) \\ \Delta\widehat{\Delta C^*}(T_3 - T_2, x, y) &= \widehat{\Delta C^*}(T_3, x, y) - \widehat{\Delta C^*}(T_2, x, y). \end{aligned} \tag{3}$$

This is essentially a second-order derivative of C^* with time and its spatial distribution shows where increasing or decreasing rates of change of C^* have been accelerating or decelerating over

a longer (20 year) period.

We also compare these spatial patterns of $\widehat{\Delta C^*}(x, y)$ and $\widetilde{\Delta C^*}(x, z)$ with those in Müller et al. (2023). One of the key differences in methodology is that Müller et al. (2023) had to consider an aggregate of available observations over each of the three time periods ($1989-1999$, $2000-2009$, and $2010-2020$) and calculate C^* referenced to a particular year for each time period (1994, 2004, and 2014, respectively). The change in ocean anthropogenic DIC, i.e., ΔC^*, was then estimated as the change between the reference years ($1994-2004$ and $2004-2014$). In contrast, because we use ECCO-Darwin model data that is regularly gridded in space and time, we are able to calculate $\Delta C^*(x, y, z)$ for each ocean grid cell more directly as a linear regression over each decade that we consider ($1993-2002$, $2003-2012$, and $2013-2022$). We also considered the same time periods as Müller et al. (2023) ($1994-2004$ and $2004-2014$) for our dataset (not shown) and found them to have similar patterns to the $1993-2002$ and $2003-2012$ time periods, so for brevity, we will only present and discuss the $1993-2002$, $2003-2012$, and $2013-2022$ periods.

2.e *Ocean Basin Mask and Regional Classification*

In order to examine spatial patterns of interannual variability in C^*, we aggregate $\Delta C^*(t_2 - t_1, x, y, z)$ over certain ocean regions. First, the global ocean is divided horizontally into five basins based on the basin mask provided by the WOA database (Locarnini et al., 2023): Atlantic, Pacific, Indian, Southern, and Arctic. This division is similar to the one used for analysis in Müller et al. (2023); however, this previous study did not provide estimates for the Arctic Ocean due to the lack of observational data. We consider the Southern Ocean separately, as it has been noted as an important region for the DIC budget (e.g., Landschützer et al., 2015; Zemskova et al., 2022) and was similarly considered separately in other studies of anthropogenic carbon (e.g., Keppler et al., 2023).

We also divide the ocean vertically; however, instead of the depth levels, we use ranges of neutral density γ (Jackett & McDougall, 1997). This is a convenient coordinate system for ocean's

isopycnals (layers of constant density) adjusted for reference pressure levels (which increase with depth). The flow and the distribution of tracers (both active tracers like temperature and passive tracers like DIC and other chemicals) primarily follows isopycnals (L. D. Talley, 2013). While the isopycnals are horizontal and align with the depth layers throughout most of the ocean, they slant towards the surface in the North Atlantic and the Southern Oceans. Therefore, it is better to divide the dynamical regions of the ocean based on neutral density rather than depth. As neutral density depends on the in-situ temperature and salinity, we use values from the WOA climatological mean (Locarnini et al., 2023) over the $1991-2020$ time period, which most closely matches the time period for the ECCO-Darwin dataset. Neutral densities were calculated using the Gibbs-Seawater (GSW) Oceanographic Toolbox (McDougall & Barker, 2017).

The neutral density ranges were taken from Müller et al. (2023) with upper bound cutoff values of

$$\begin{aligned}\gamma = \quad & [26.00, 26.50, 26.75, 27.00, 27.25, 27.50, 27.75, \\ & 27.85, 27.95, 28.05, 28.10, 28.15, 28.20, 30]\,\mathrm{kg/m^3}. \end{aligned} \tag{4}$$

The GSW function for computing neutral densities does not cover the Arctic Ocean, so we consider it as one region without any further vertical divisions. The other four ocean basins are further divided into regions based on neutral density values. We adjust the neutral density cutoffs such that at any given timestep, there are at least 2000 grid points within a region to ensure that there are enough points for the aggregate analysis. This yields 11 regions within the Southern Ocean basin with neutral density cutoffs of

$$\gamma = [27, 27.25, 27.50, 27.75, 27.85, 27.95, 28.05, 28.10, 28.15, 28.20, 30]\,\mathrm{kg/m^3}$$

and 11 regions within each of the Atlantic, Pacific, and Indian Ocean basins with neutral density cutoffs of

$$\gamma = [26, 26.50, 26.75, 27, 27.25, 27.50, 27.75, 27.85, 27.95, 28.05, 30]\,\mathrm{kg/m^3}.$$

A range of $\gamma < 26$ kg/m^3 corresponds to the neutral density layer located between the surface and 150 m at the subtropical latitudes. As a result, the five ocean basins are separated into 45 regions in total.

2.f *EOF analysis for interannual variability*

The monthly temporal resolution of our data before averaging allows us to examine patterns of interannual variability in further detail. Specifically, we conduct the EOF analysis of the monthly maps of vertically-integrated $\Delta C^*(t_2 - t_1, x, y, z)$. This analysis allows us to identify spatial (EOFs) and temporal (Principal Component (PC) timeseries) patterns that drive interannual variability in ΔC^* and compare them to the known climatological modes. The analysis is performed using xeof package for Python (Rieger & Levang, 2024). Larger rates of change of C^* have been found to be predominantly within the top 1500 m both in previous studies (e.g., Keppler et al., 2023) and in this study (see § 3.a.2). Therefore, the analysis is focused on ΔC^* vertically integrated over this depth range. We also limit our analysis to the $1995-2022$ period to exclude any influence from potential ECCO-Darwin spin-up bias for $1992-1994$ that has been previously noted (Carroll et al., 2022). The EOFs and PCs are computed after the long-term trend and season cycles are removed from the vertically-integrated ΔC^* at each grid cell (x, y).

After the top four EOFs and the corresponding PCs are computed, we compare them to the six known global climate variability modes based on Messié and Chavez (2011), namely the El Niño Southern Oscillation (ENSO) (NOAA Physical Sciences Laboratory, 2025b), North Pacific Gyre Oscillation (NPGO) (NOAA Physical Sciences Laboratory, 2025c), Pacific Decadal Oscillation (PDO) (NOAA National Centers for Environmental Information, 2025), El Niño Modoki (JAMSTEC, 2025), Atlantic Niño (NOAA Climate Prediction Center, 2025), and Atlantic Multidecadal Oscillation (AMO) (NOAA Physical Sciences Laboratory, 2025a). Spatial patterns of the EOFs are compared to the global modes of sea surface temperature variability (Messié & Chavez, 2011) that have been shown to align well with these six climate indices. For a more quantitative analysis, we also compute the lag correlation of the PC timeseries with the time-

series of each of the monthly climate indices, as we expect that there might be some lag in the ocean carbon response to climate mode variability. As we expect the climate mode variability to lead the variability in the ocean C^* changes, we take the cross-correlation value with the largest magnitude and positive lag for each climate mode. Climate modes with largest cross-correlation values are expected to be most likely to explain the interannual variability in ΔC^*.

3 Results

3.a *Decadal variability of* $\boldsymbol{C^*}$

First, we will examine the longer decadal changes in ocean anthropogenic DIC concentrations for three decades: $1993-2002$ (denoted as T_1), $2003-2012$ (T_2), and $2013-2022$ (T_3). Vertically-integrated decadal changes $\widehat{\Delta C^*}(T,x,y)$ are presented in § 3.a.1 and zonally-averaged changes $\widetilde{\Delta C^*}(T,x,z)$ in § 3.a.2.

3.a.1 Vertically-averaged decadal changes in C^*

All decades show widespread increasing trends in ocean anthropogenic DIC concentration ($\widehat{\Delta C^*} > 0$) in Figure 1(a-c)). There are several areas that stand out with larger increasing rates, many within the Eastern Boundary Current regions. In the Atlantic region, the large increasing trends ($\widehat{\Delta C^*} \approx 18.0$ mol m^{-2} dec^{-1}) appear over the North Atlantic along the Gulf Stream and between $45-65$°N, and along the east coast of South America within the Brazil Current region ($20-50$°S). In the Pacific Ocean, we find the large increasing rates in the northern part along the Kuroshio and in the equatorial region ($5-10$°N) along the equatorial currents. In the Indian ocean, the region south of Australia ($300-330$°E longitude, around $30-50$°S) has large $\widehat{\Delta C^*}$ values. The temporal trends in ocean carbon storage in the Southern Ocean are predominantly positive, though not exceeding 20 mol m^{-2} dec^{-1}, whereas in many parts of the Arctic ($50-320$°E band), $\widehat{\Delta C^*} \geq 20$ mol m^{-2} dec^{-1}. Overall, we find these regions with larger positive values of $\widehat{\Delta C^*}$ to align with those identified by Gruber et al. (2019) and Müller et al.

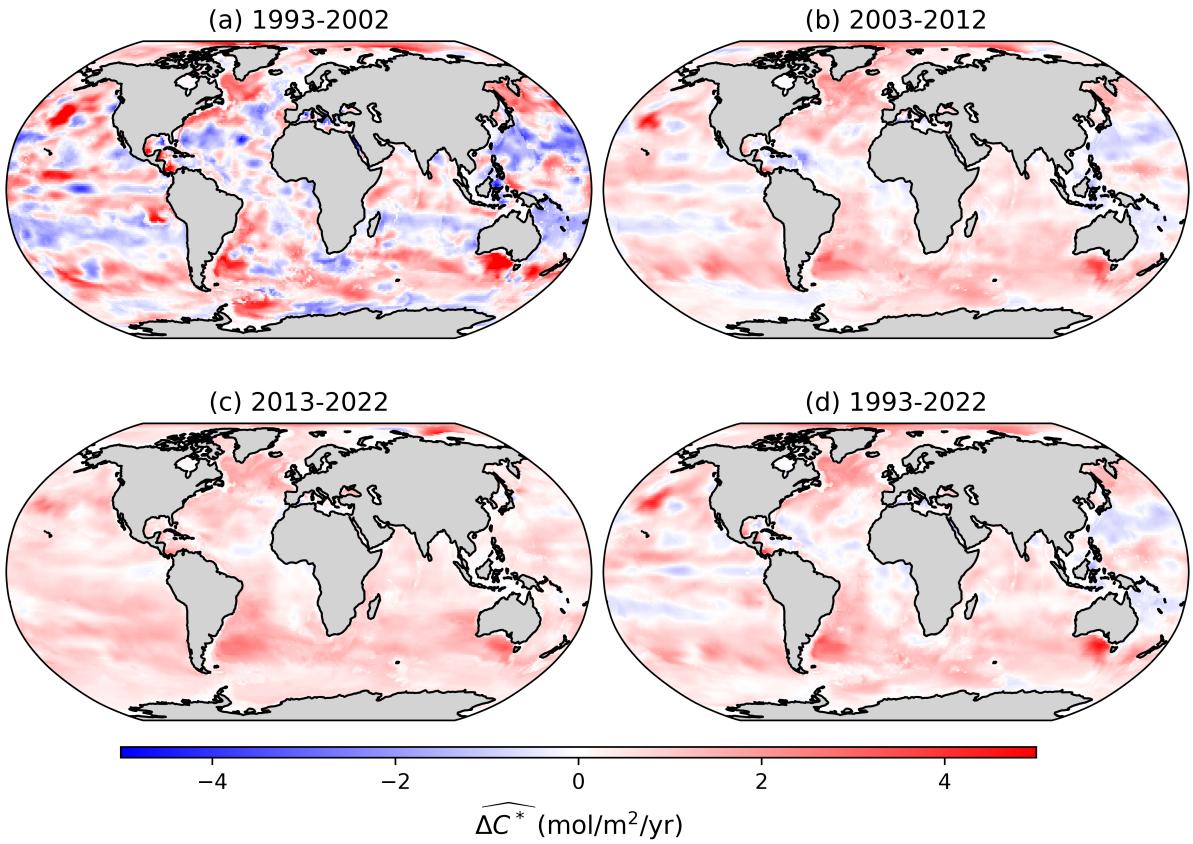

Fig. 1 Vertically-integrated decadal changes in ocean anthropogenic carbon inventory $\widehat{\Delta C^*}$ for three decades separately (a) $1993-2002$ (T_1), (b) $2003-2012$ (T_2), (c) $2013-2022$ (T_3), and (d) the full period $1993-2022$. Positive (negative) values correspond to overall increase (decrease) in ocean anthropogenic carbon concentrations. Land is shaded in grey.

(2023), though the magnitude of our values is larger by up to a factor of two.

The decreasing trends are predominantly noticeable in the $1993-2002$ time period, and the area with decreasing trends diminishes with time, such that $\widehat{\Delta C^*} > 0$ almost everywhere in the last decade ($2013-2022$). Over the $1993-2002$ time period, regions with $\widehat{\Delta C^*} < 0$ are predominantly found in the centers of subtropical gyres within the $10-30^\circ$ latitudinal bands in both Northern and Southern Hemispheres throughout the North Atlantic, South Pacific, South Indian, and western part of the North Pacific Ocean regions. Interestingly, these latitudinal bands with $\widehat{\Delta C^*} < 0$ are not as coherent in the Southern Atlantic Ocean, where there is a strong signal of increasing ocean anthropogenic DIC concentrations off the coast of South America. Regions with large magnitude of decreasing anthropogenic DIC trends in the ocean were not previously reported in Gruber et al. (2019) and Müller et al. (2023). It is possible that they

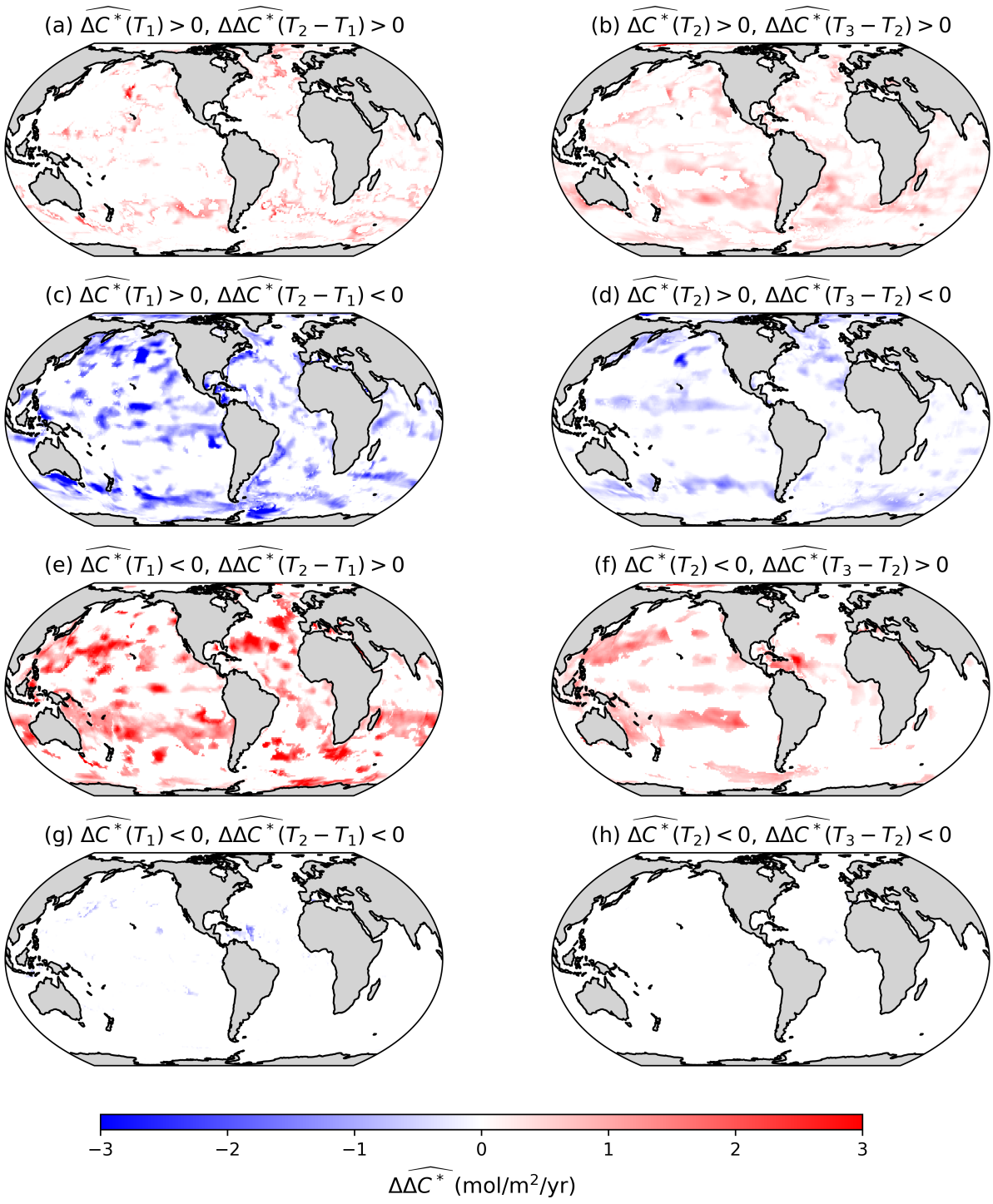

Fig. 2 Comparison of decadal differences in the rates of change anthropogenic carbon storage. The maps show the decadal differences in the vertically-integrated ocean anthropogenic carbon inventory $\widehat{\Delta C^*}$ ($\Delta\widehat{\Delta C^*}$), that is difference between: (a, c, e, g) 2003–2012 (T_2) and 1993–2002 (T_1), and (b, d, f, h) 2013–2022 (T_3) and 2003–2012 (T_2). Subplots are separated by the sign of $\Delta\widehat{\Delta C^*}$ and $\widehat{\Delta C^*}$ of the first period: (a, b) $\Delta\widehat{\Delta C^*} > 0$, $\widehat{\Delta C^*} > 0$, (c, d) $\Delta\widehat{\Delta C^*} < 0$, $\widehat{\Delta C^*} > 0$, (e, f) $\Delta\widehat{\Delta C^*} > 0$, $\widehat{\Delta C^*} < 0$, and (g, h) $\Delta\widehat{\Delta C^*} < 0$, $\widehat{\Delta C^*} < 0$. The color in each subplot corresponds to the value of $\Delta\widehat{\Delta C^*}$. Land is shaded in grey.

are in part an artifact of large negative ΔC^* during the ECCO-Darwin model spin-up period in $1992-1994$ as discussed below in § 3.b. However, observational data in the 1990s was not spatio-temporally well-distributed. For example, most of observations used for the interpolation for the $1989-1999$ time period in the Indian Ocean was from 1995 and in the North Atlantic was from 1997 with generally fewer data points available prior to 1994 (Gruber et al., 2019; Müller et al., 2023). The shipboard DIC measurements used in these previous studies were also predominantly taken during the warmer months (late spring, summer, early fall) (Keppler et al., 2020). Therefore, it is possible that the previous studies were not able to accurately capture temporal variability of ocean DIC due to observational biases and data sparsity, and thus not able to capture $\Delta C^* < 0$ in the subtropical regions that we find here.

We also find that in the Pacific and Indian Ocean sectors ($150-360$°E longitude) of the Southern Ocean near Antarctica (≈ 70°S), there is a latitudinal band with a decreasing trend in anthropogenic carbon storage (approximately -15 mol m^{-2} dec^{-1}). This, overall, agrees with the regions of decreasing ocean DIC concentrations below 500 m depth in the Southern Ocean in $1993-1993$ found by Zemskova et al. (2022). This finding also agrees with Gruber et al. (2019), who found lower than expected accumulation of ocean anthropogenic DIC in this region.

Based on the sign of the decadal differences $\Delta\widehat{\Delta C^*}$ and decadal trends $\widehat{\Delta C^*}$, we can divide the temporal patterns into four categories. Using decadal periods T_1 and T_2 as examples:

(1) $\Delta\widehat{\Delta C^*}(T_2 - T_1) > 0$ and $\widehat{\Delta C^*}(T_1) > 0$ indicate an acceleration in the increasing rates of ocean carbon storage (Fig. 2(a));

(2) $\Delta\widehat{\Delta C^*}(T_2 - T_1) < 0$ and $\widehat{\Delta C^*}(T_1) > 0$ for the first decadal period indicating a deceleration in the increasing rates or possibly a shift to decreasing rates of ocean carbon storage (Fig. 2(c));

(3) $\Delta\widehat{\Delta C^*}(T_2 - T_1) > 0$ and $\widehat{\Delta C^*}(T_1) < 0$ for the first decadal period indicating a deceleration in the decreasing rates or possibly a shift to increasing of ocean carbon storage (Fig. 2(e));

(4) $\Delta\widehat{\Delta C^*}(T_2 - T_1) < 0$ and $\widehat{\Delta C^*}(T_1) < 0$ for the first decadal period indicating an acceleration in the decreasing rates of ocean carbon storage (Fig. 2(g)).

Same applies to periods T_2 and T_3 (Fig. 2(b,d,f,h)).

Considering the decadal shift from the 1990s to the 2000s ($\Delta\widehat{\Delta C^*}(T_2 - T_1, x, y)$), we observe a pattern of compensation in ocean anthropogenic DIC uptake. Specifically, slowdown in the increasing rates of C^* (category 2, Fig. 2(c)) is found along the Eastern Boundary Currents (e.g., the Gulf Stream, Kuroshio, and Brazil Current), patch south of Australia, and many parts of the Antarctic Circumpolar Current. In contrast, within the subtropical gyres and near Antarctica in the Pacific and Indian sectors of the Southern Ocean where ocean carbon storage has been decreasing in the 1990s, there has been possibly a shift to taking up more DIC with a potential switch from negative to positive $\widehat{\Delta C^*}$ (category 3, Fig. 2(e)).

Going from the 2000s to 2010s ($\Delta\widehat{\Delta C^*}(T_3 - T_2, x, y)$), data points that fall into category 1, i.e., with accelerating increasing rates of C^*, are more wide-spread (Fig. 2(b)). This suggests the reinvigoration of ocean carbon sink and generally more accelerated uptake of anthropogenic DIC by the ocean over the last two decades. Spatial patterns for regions in categories 2 (Fig. 2(d)) and 3 (Fig. 2(f)) have similar patterns to the distribution of $\Delta\widehat{\Delta C^*}(T_2 - T_1, x, y)$, but the magnitude and area covered by regions that fall into these categories is smaller for the $2003 - 2022$ period.

Finally, we acknowledge the temporal division of the data into decades is somewhat arbitrary based on the length of the available data and does not necessarily correspond to any particular natural ocean decadal cycles. Therefore, we show the total linear trend in vertically-integrated ocean storage of anthropogenic carbon from 1992 to 2022 in Figure 1(d). Spatial distribution of significantly increasing and decreasing trends are similar to those in the decade 2003-2012 (see Fig. 1(b)).

3.a.2 Zonally-averaged decadal changes in C^*

Figure 3 shows the zonally-averaged ΔC^* (denoted as $\widetilde{\Delta C^*}$) across latitude and depth for each major ocean basin over the period 1992–2022, showcasing the meridional and vertical patterns of C^* accumulation. The rate of change of C^* is predominantly positive in all basins with a few notable areas of decreasing ocean anthropogenic DIC ($\widetilde{\Delta C^*} < 0$). These regions are

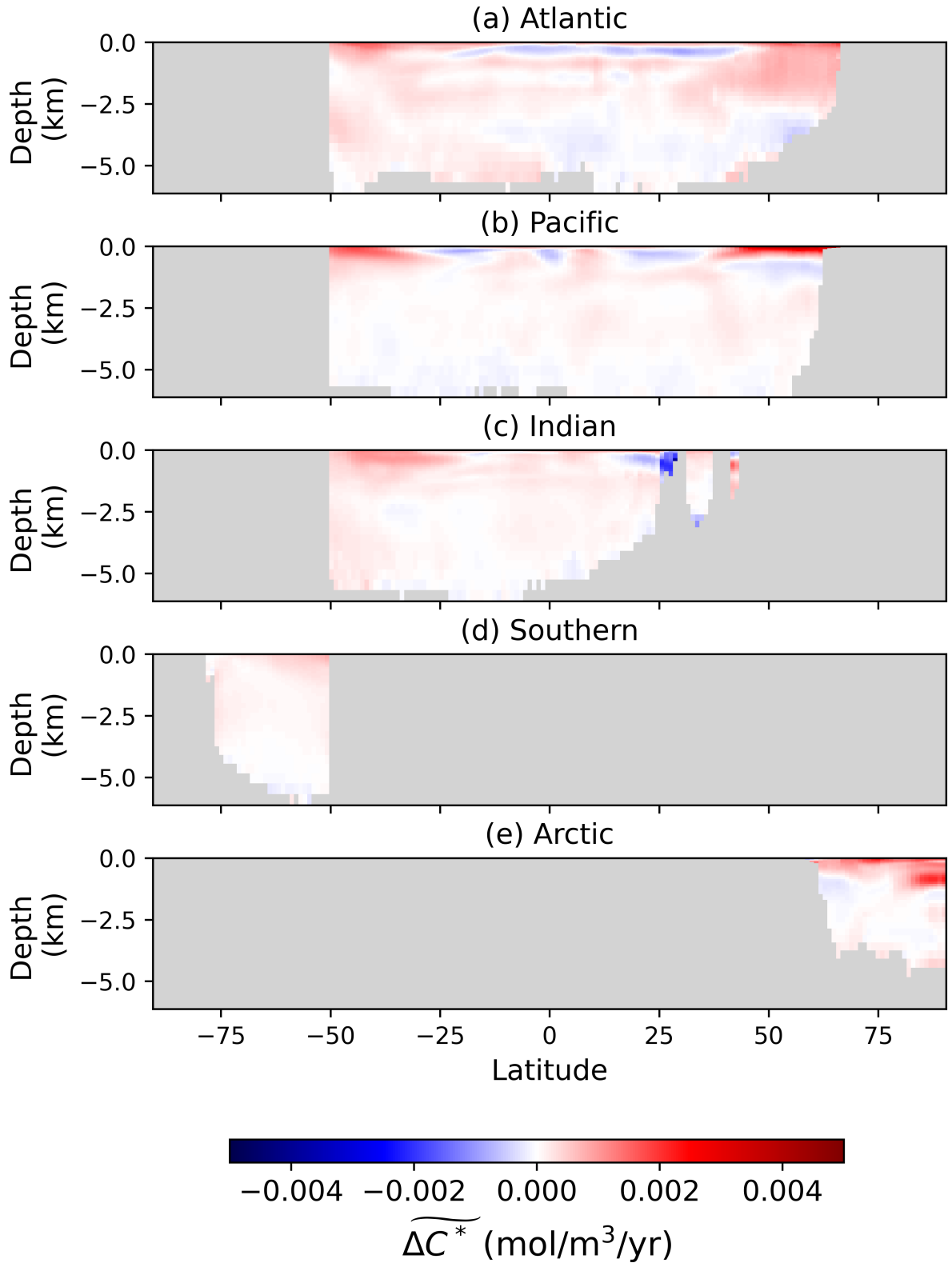

Fig. 3 Zonally-averaged trends of ocean anthropogenic carbon concentrations ($\widetilde{\Delta C^*}$) from 1992 to 2022 in five basins: (a) Atlantic, (b) Pacific, (c) Indian, (d) Southern, and (e) Arctic. Positive (negative) values indicate an increasing (decreasing) anthropogenic carbon concentrations at that latitude–depth position. Land is shaded in grey.

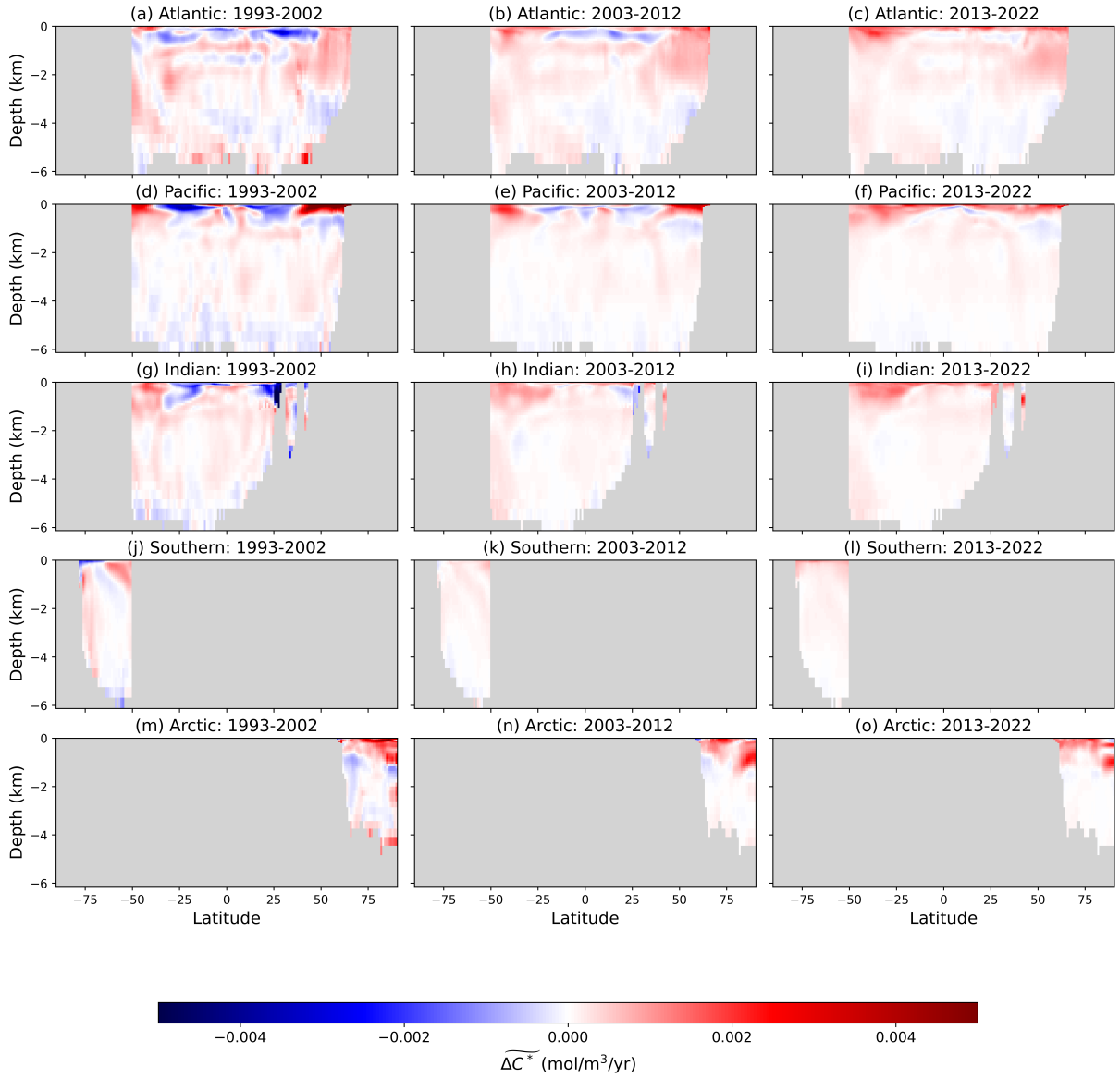

Fig. 4 Same as Figure 3 but broken down into decadal trends: (a-e) 1993 – 2002, (f-j) 2003 – 2012, (k-o) 2013 – 2022.

predominantly in the centers of subtropical gyres in the upper ($\approx$ 500 m) Pacific and Indian Oceans and the subsurface Atlantic Ocean. Considering the breakdown of $\widetilde{\Delta C^*}$ into decades, these decreasing C^* trends are largest in magnitude in the 1990s (Fig. 4(a, d, g, j, m)); however, by the 2010s, these regions of the ocean also exhibit increasing C^* trends (Fig. 4(c, f, i, l, o)). Similar decreasing C^* trends ($\widetilde{\Delta C^*} < 0$) in the tropical and equatorial Atlantic (e.g., 1994 – 1998 for $\gamma > 27$ kg/m^3 in Fig. 5) point to the influence of lower latitude upper ocean circulation cell (L. D. Talley, 2013). There is also the region between 1 and 2 km depth in the Atlantic with

$\widetilde{\Delta C^*} < 0$ in the 1990s for the AMOC density layers noted in Fig. 5 and corresponding $\widetilde{\Delta C^*} < 0$ along the upwelling isopycnals in the Southern Ocean.

By the last decade of the analysis period ($2003 - 2022$), we find $\widetilde{\Delta C^*}$ to be predominantly positive in all basins and at all depths. The largest rate of increase is within the upper ocean ($500 - 1000$ m) and within the deep water formation and sinking of North Atlantic Deep Water. In particular, large positive $\widetilde{\Delta C^*}$ trends are found in the upwelling regions of the subtropical South Pacific and Indian Oceans (Fig. 4(i, f)). This is consistent with relatively larger positive trends in the upper ocean and negligible change in ocean anthropogenic DIC reported by Keppler et al. (2023) and Müller et al. (2023). This result also points to ocean anthropogenic carbon predominantly being confined to the upper ocean circulation cell where it can more easily exchange with the atmosphere rather than being stored in the lower circulation cell with longer residence times.

3.b *Interannual variability of* $\boldsymbol{C^*}$

We now examine shorter-term change in the oceanic storage of anthropogenic carbon (C^*), namely a year-to-year change. Figure 5 shows ocean $\Delta C^*(t_1, t_2)$, where t_1 and t_2 are two consecutive years, in different ocean basins over the $1992 - 2022$ period with detailed information over different neutral density ranges (proxy for depth layers), i.e., for the 45 different ocean basins described in § 2.e. Overall, we find a predominantly positive trend in all five ocean basins for the year-to-year changes of ΔC^* ($\Delta C^* > 0$), indicating a general increase in the ocean storage of anthropogenic carbon over the analyzed period. In particular, after 2012, $\Delta C^* > 0$ for almost all γ layers. Unlike other ocean basins that have intermittent periods of decreasing C^* trends, the Arctic Ocean exhibits increasing ocean DIC trends over the entire time range. Overall, the rates of largest magnitude are in shallower (less dense) layers, whereas we find mostly weakly positive trends in the denser γ layers, suggesting less anthropogenic DIC accumulation in the deeper ocean. Figure 5 exhibits intermittency in the sign and magnitude of ΔC^*, which suggests that interannual variability in the ocean DIC is important when considering changes in the ocean's

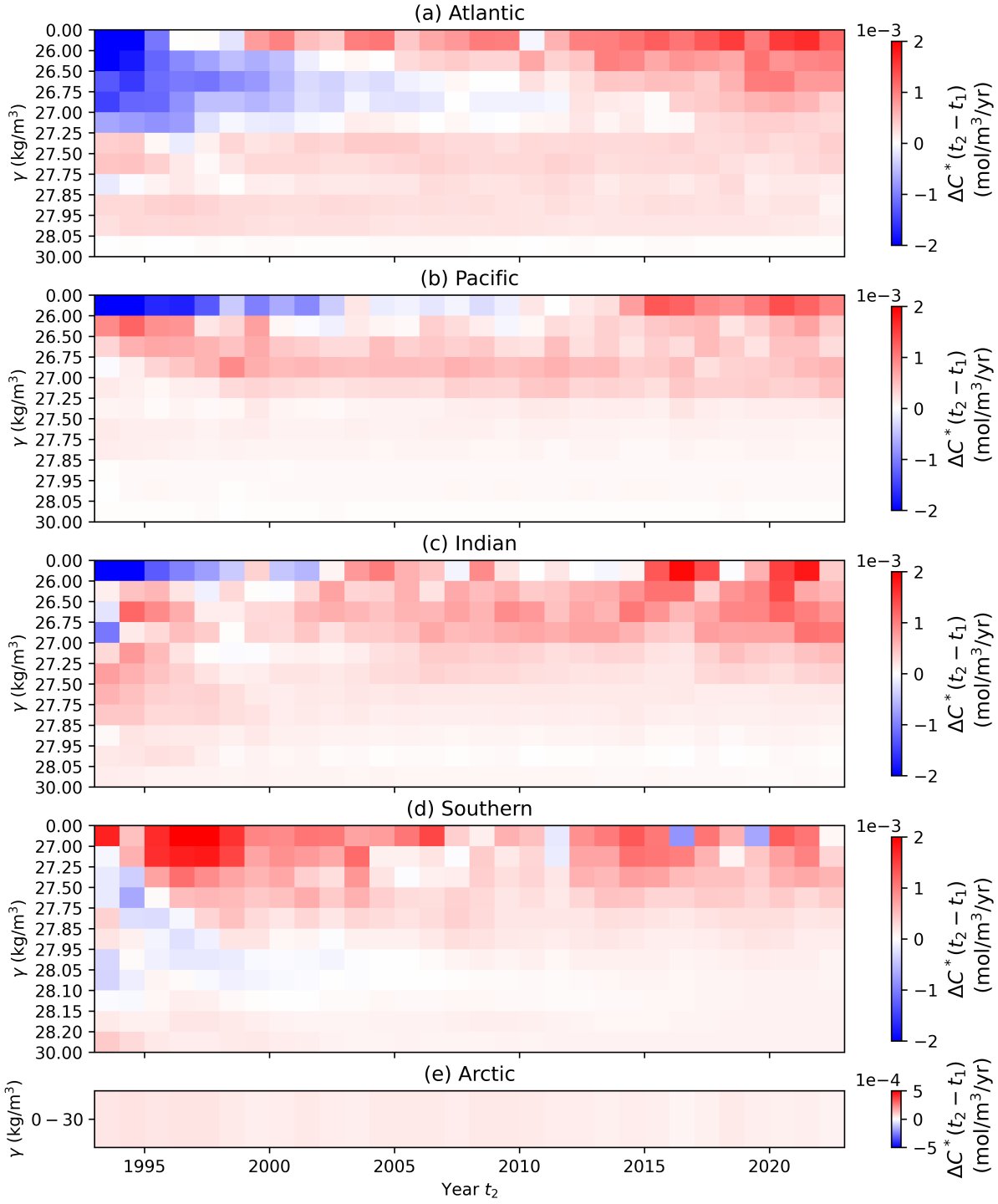

Fig. 5 Year-to-year changes in C^* ($\Delta C^*(t_2 - t_2)$) from 1992 to 2022 across five ocean basins: (a) Atlantic, (b) Pacific, (c) Indian, (d) Southern, and (e) Arctic oceans. The four ocean basins except the Arctic are further subdivided into neutral density layers (see § 2.e for details). Note the differences in the colorbar for (e). The red colors represent increases ($\Delta C^* > 0$), and the blue colors represent decreases ($\Delta C^* < 0$) in the ocean anthropogenic DIC concentrations averaged over the particular ocean subregion.

ability to take up more atmospheric carbon.

The ΔC^* timeseries in Figure 5 also reveals connectivity of certain ocean basins through global ocean circulation. Specifically, we find negative ocean DIC trends propagating from near the surface (lower values of γ) into the ocean interior (larger values of γ) in the Atlantic over the $1992-2005$ period (Fig. 5(a)). These γ layers are in the range of Mode Water and Intermediate Water, suggesting a decrease in the anthropogenic DIC uptake and delivery into the ocean interior in the North Atlantic, potentially due to weakening Atlantic Meridional Overturning Circulation (AMOC) (Gruber et al., 2019; Pérez et al., 2013). With a slight temporal delay, we find decreasing trends within the Antarctic Intermediate Water (AAIW, $\gamma \in [27, 27.5]$ kg/m^3) that are then transported to denser Circumpolar Deep Water (CDW, $\gamma \in [27.5, 28]$ kg/m^3) ranges, most likely within the upwelling region in the Southern Ocean that is part of the AMOC cell (Fig. 5(d)). Analyzing the annual rather than decadal changes in C^* over the different γ layers allows us to better track and attribute trends to the ocean circulation patterns.

Interestingly, we find that over the similar period ($1995-1999$), C^* in the lighter γ ranges in the Southern Ocean ($\gamma \leq 27.5$ kg/m^3) was increasing at a high rate. These trends, indicative of possible DIC saturation in near-surface ocean layers, align with the previous findings of faster increase in surface ocean CO_2 compared to the atmosphere and thus a decreasing ocean DIC sink in the 1990s by Landschützer et al. (2015). While ΔC^* is still positive in those γ layers in the 2000s, the magnitude is lower consistent with the reinvigoration of the Southern Ocean carbon sink (Landschützer et al., 2015). These trends in the 1990s also suggest a compensation by the Southern Ocean to take up additional anthropogenic carbon during the period of reduction of such uptake in the North Atlantic, also noted in previous studies (Gruber et al., 2019; Müller et al., 2023). We do not find such compensation in later periods as ΔC^* is almost uniformly positive; however, it is possible that this is part of a longer-term ocean circulation patterns that are not fully captured in the 30 years analyzed here.

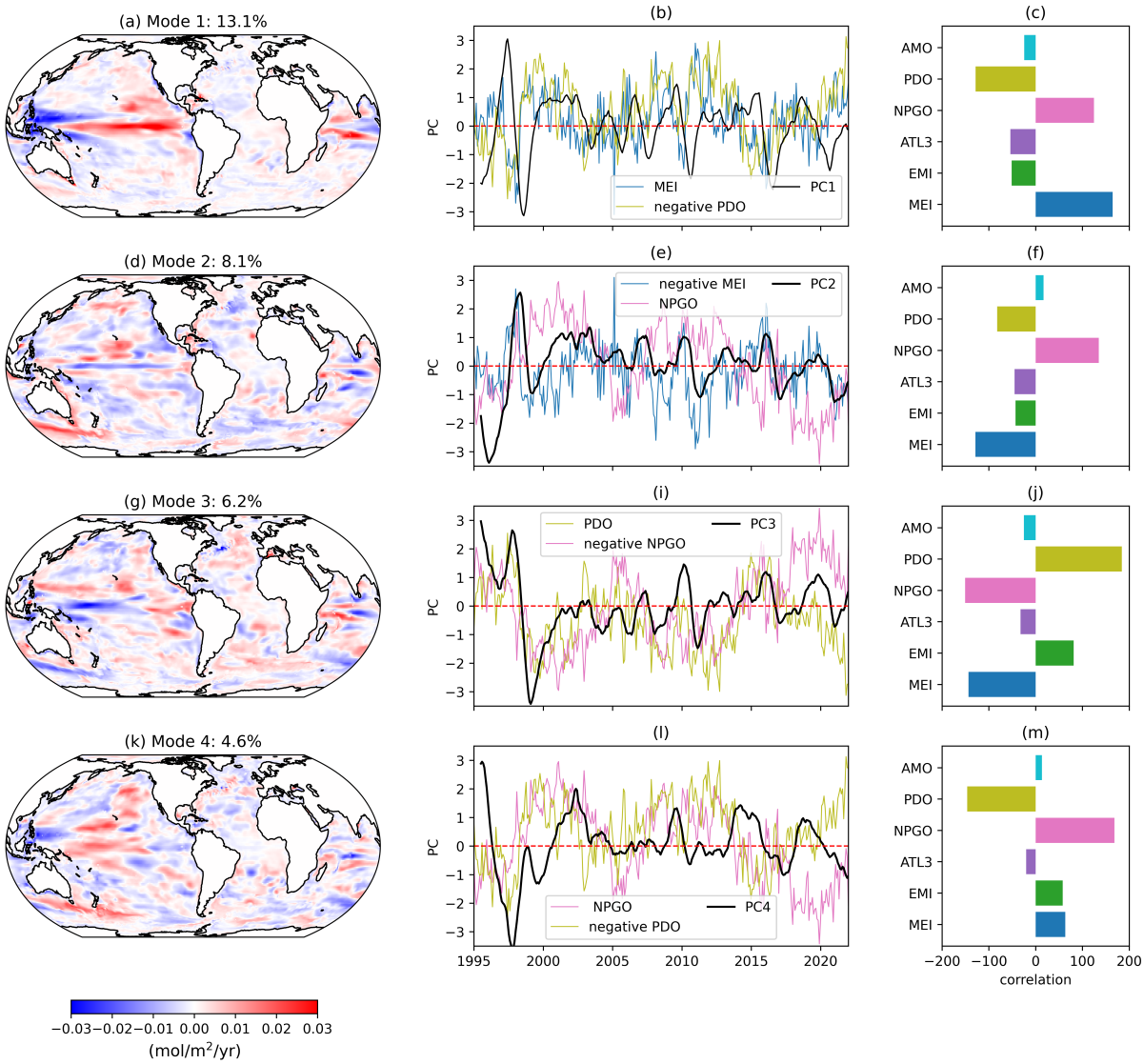

Fig. 6 (a, d, g, k) EOFs; (b, e, i, l) PC timeseries; and (c, f, j, m) correlation of PC timeseries with climate mode indices for the first four modes for vertically-integrated ΔC^* variability. Indices for the two fitting climate modes based on correlation are also plotted: (b) Multivariate ENSO Index (MEI) and negative of Pacific Decadal Oscillation (PDO), (i) negative MEI and North Pacific Gyre Oscillation (NPGO), (l) NPGO and negative PDO.

3.c *EOF analysis of Interannual Variability of* $\boldsymbol{\Delta C^*}$

We now use EOF analysis to further investigate the spatio-temporal patterns of the interannual variability of ΔC^*. The first four modes for the variability of ΔC^* vertically integrated over the top 1500 m, which capture about 32% of interannual variability, are shown in Figure 6. Because the distribution of carbon in the ocean is not only governed by circulation (Carroll et al., 2022) and there are most likely lags in the response of carbon distribution to changes in circulation due

to climatological modes, the EOFs and PC timeseries are not exactly aligned with the known climatological modes and indices and show patterns of a combination of several climatological modes. This can be inferred from the fact that for each PC timeseries, there are multiple climate modes with similar magnitude of cross-correlation (Fig. 6(c, f, j, m)) rather than one climate mode being dominant. Nonetheless, based on the prominent spatial features and comparison of PC timeseries with monthly climate index timeseries, we can approximately attribute these ΔC^* variability modes to the known climate modes.

The first mode EOF resembles the ENSO mode (Fig. 6(a)) and PC1 timeseries roughly aligns with the Multivariate ENSO Index (MEI) (NOAA Physical Sciences Laboratory, 2025b) (Fig. 6(b)) that has the largest cross-correlation value (Fig. 6(c)). The PC timeseries is also strongly correlated with the PDO mode, which is perhaps not surprising as part of the PDO anomaly is forced by the ENSO variability (Schneider & Cornuelle, 2005). The second mode is more difficult to attribute to a particular climate mode based on the EOF spatial structure alone (Fig. 6(d)), though the PC timeseries is generally negatively correlated with ENSO (Fig. 6(e-f)). For the third and fourth modes, PDO and NPGO are the most correlated climate indices (Fig. 6(j, m)) and the EOF spatial patterns also resemble these climate modes: dipole in the North Pacific for PDO and dipole between the North Pacific and Indian Ocean for NPGO (Fig. 6(g, k)). The main differences between these two modes are the sign of the correlation coefficient and the longer lag for the fourth mode (2 years for PDO and 1.5 years for NPGO) compared with the third mode (almost zero lag for both PDO and NPGO). Overall, this analysis reveals that about a third of the interannual variability in the rate of change ΔC^* in the top 1500 m is primarily driven by three different Pacific climatological modes.

3.d *Total* $\boldsymbol{C^*}$ *Change*

Now that we have examined the spatial distribution of the rates of change of ocean anthropogenic DIC concentrations, we provide estimates in ΔC^* integrated over the entire ocean. We compare our results with several previous estimates: (1) 51 ± 11 Pg C change of DIC in the ocean from

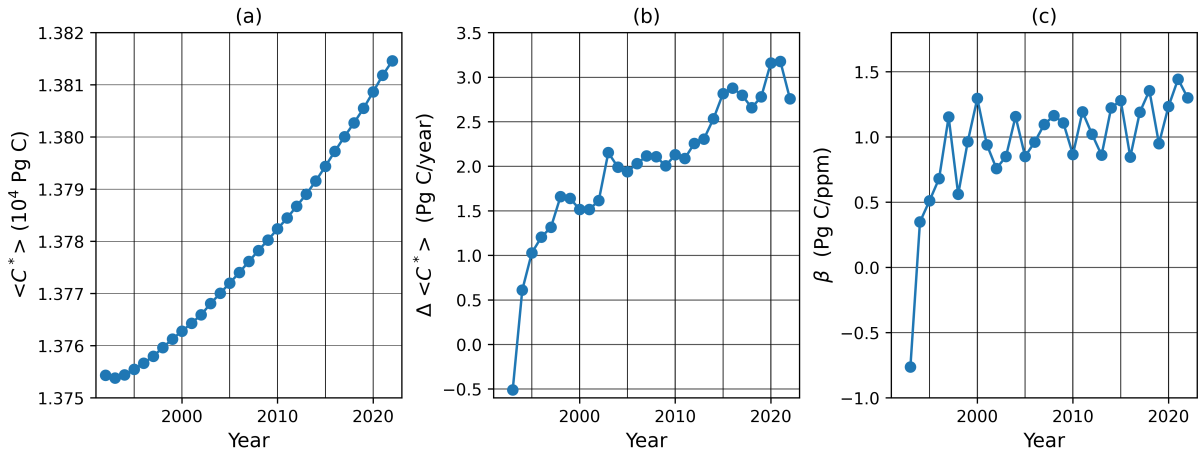

Fig. 7 (a) Annual globally-integrated anthropogenic carbon concentration ($\langle C^* \rangle$) from 1992 to 2022, (b) annual rate of change of $\langle C^* \rangle$, (c) ratio of $\langle C^* \rangle$ to global annual mean atmospheric CO_2 concentrations.

2004 to 2019 based on a machine-learning model interpolation of observational data (Keppler et al., 2023), (2) $44 - 49$ Pg C change in anthropogenic ocean carbon based on interpolated observational data over $2004 - 2019$ (Gruber et al., 2019; Keppler et al., 2023), and (3) 64 Pg C change in total ocean DIC over the $1995 - 2017$ time period based on ECCO-Darwin model output (Carroll et al., 2022) that we also use in this study..

Figure 7(a) shows C^* integrated over the entire global ocean (denoted as $\langle C^* \rangle$) from 1992 to 2022. Estimated from Friedlingstein et al. (2022), the total anthropogenic emissions from 1992 to 2022 is approximately 216 PgC, so the portion of the ocean absorption of anthropogenic carbon is around 28%. This value is within the range of $31 \pm 7\%$ found by Keppler et al. (2023) over the $2004 - 2019$ time period. Over the $2004 - 2019$ period, the ECCO-Darwin estimate of the increase in anthropogenic carbon storage (C^*) is 36 Pg C, which is smaller than the total DIC change of 51 ± 11 Pg C reported by Keppler et al. (2023) and closer to the anthropogenic portion (44–49 Pg C ±6 Pg C) inferred from the C^* estimates of Gruber et al. (2019). For $1995 - 2017$, the output of the ECCO-Darwin model estimates an anthropogenic $\langle C^* \rangle$ increase of 45 Pg C, which is smaller than the total DIC change of 64 Pg C reported by Carroll et al. (2022), but consistent with the expectation that C^* represents only the anthropogenic portion of the total DIC. The total amount of ocean carbon of anthropogenic origin (integrated C^*) is about 37% of

the total DIC pool estimated by Carroll et al. (2022). However, $\Delta\langle C^* \rangle$ is approximately 70% of the total DIC change, suggesting that a significant portion of the ocean carbon budget imbalance is influenced by the uptake of anthropogenic emissions.

The linear rate of increase in $\langle C^* \rangle$ calculated over the entire $1992 - 2022$ period is about 1.9 Pg C yr^{-1}, which is lower than the 3.2 ± 0.7 Pg C yr^{-1} rate estimated by Keppler et al. (2023). However, consistent with Carroll et al. (2022), who found that the global DIC tendency is increasing over 1995 to 2019, our total C^* trend (Figure 7(b)) also exhibits an accelerating trend rather than a constant linear increase. This implies that the rate of oceanic anthropogenic carbon uptake ($d\langle C^* \rangle/dt$) is not constant. This result reflects the combined effects of increased atmospheric CO_2 concentrations and some potential changes in ocean circulation and ventilation. It should be noted that there could also be some residual model spin-up bias in the early part of the timeseries ($1992 - 1994$) (Carroll et al., 2022), so these earlier results, e.g. $d\langle C^* \rangle/dt < 0$, should be interpreted with caution. To account for atmospheric change, we also compute β, which is the ratio of $\langle C^* \rangle$ to the annually-averaged atmospheric CO_2 concentrations (Lan, Tans, & Thoning, 2025) (Figure 7(c)). During most of our analysis period, we find β to fluctuate over the $0.5 - 1.5$ Pg C/ppm range with noticeable interannual variability, possibly due to many long-term ocean and atmospheric circulatory patterns. This further suggests the need for a more careful investigation of ocean DIC at finer temporal resolution (seasonal/annual) rather than decadal averages that may not align with any particular circulation cycles.

4 Limitations

While this study provides a basin-scale, decadal assessment of anthropogenic carbon trends using a physically consistent and spatially complete ECCO-Darwin model product, several limitations should be acknowledged. First, our specific methodology to separate the natural and anthropogenic carbon concentrations following previous works (Gruber et al., 2019; Müller et al., 2023) uses fixed stoichiometric ratios (e.g., C:P and C:N) for calculation. This may introduce

regional biases, especially in areas where C:P deviates from the global Redfield average (Deutsch & Weber, 2012; Liefer et al., 2024; Martiny et al., 2013; Seelen et al., 2025) and omits possible effects of temporal changes in these stoichiometric ratios over such a long timeseries (Hutchins & Tagliabue, 2024; Liu et al., 2025).

Second, The ECCO-Darwin model has to parameterize any small-scale processes that occur at spatial scales smaller than the grid resolution and temporal scales smaller than the model time step (1200 s), which can introduce model biases. We attempt to mitigate this problem by focusing on annually-averaged and spatially-integrated values to smooth over any small-scale biases. However, the use of annual-mean data restricts the resolution of seasonal and short-term variability (Keppler et al., 2020). The absence of high-frequency (e.g., monthly or daily) data limits our ability to resolve fine-scale dynamics and may underestimate short-term variability that affects ocean carbon concentrations (Mahadevan, Lévy, & Mémery, 2004).

Finally, while the ECCO-Darwin model helps address data sparsity in under-observed regions such as the Arctic, it does not replace direct observations. While the model has demonstrated a good agreement overall between the individual output values of PO_4, DIC, and alkalinity and observed values at the same time and location (see Fig. 2 in Carroll et al. (2020)), C^* computed here is a combination of these variables, and thus the error would propagate. Further model-data uncertainty analysis is needed to assess the interannual variability and trends in C^* presented here. Because the ECCO-Darwin model output is deterministic and the current version does not provide the outputs needed to evaluate the agreement between model solutions and in-situ observations for the three-dimensional variables, we are unable to incorporate uncertainty quantification into our analysis, which limits the statistical interpretation of differences across time periods or basins. However, the model has been extensively validated for the surface ocean partial CO_2 pressure and air-sea CO_2 flux both spatially and temporally against data-based reconstructions and has been show to have interannual variability that is more consistent with these data-based products compared to other ocean biogeochemical models Carroll et al. (2020). The data assimilation approach of the ECCO-Darwin model that minimizes the drift and bias

of the model solution gives further confidence in using the output. Nonetheless, the magnitude and spatio-temporal distribution of the discrepancies between the model and observations for DIC and C^* will need to be quantified, especially in investigating long temporal trends, once such outputs become available.

5 Discussion and Conclusions

In this study, we present an assessment of interannual and decadal changes in anthropogenic carbon storage in the global ocean from 1992 to 2022, using physically and biogeochemically consistent modeled data from the ECCO-Darwin ocean state estimate (Carroll et al., 2020). The ECCO-Darwin assimilates biogeochemical observations and has shown to have good agreement with GLODAP observational data for DIC (Carroll et al., 2022) making it a good candidate for this analysis. We estimate the portion of ocean DIC attributable to the ocean's uptake of anthropogenic CO_2 from the atmosphere using the quasi-steady tracer C^* used in previous studies (Clement & Gruber, 2018; Gruber et al., 2019; Müller et al., 2023). However, compared to these prior studies (Gruber et al., 2019; Müller et al., 2023), our approach offers two key extensions. One is that our analysis spans over three decades, with one more recent decade from 2012 to 2022. The other is that because of the higher temporal resolution of the ECCO-Darwin model data, we are able to examine the interannual variability in the changes in C^* and more accurately estimate decadal trends using linear regression rather than aggregating data over a decade and computing decadal differences.

Over the full 1992–2022 period, we estimate a total global ocean C^* increase of approximately 60 Pg C, corresponding to about 28% of total anthropogenic CO_2 emissions during this time, which is consistent with previous estimates over the $2004 - 2019$ time period (Keppler et al., 2023) . The general trend of temporal changes in C^* shows a nonlinear increase both exhibiting interannual variability and accelerating trend. In the last decade of our analysis ($2012 - 2022$), the rate of C^* increase is within the range of 3.2 ± 0.7 Pg C/year previously estimated based on

observational data (Keppler et al., 2023), but in earlier decades, the rate is below 2 Pg C/year.

To account for the exponentially rising atmospheric CO_2 concentrations, we compute the ratio β of the rate of change of globally-integrated C^* to the rate of change of atmospheric CO_2 concentration. Over $1995-2022$, our analysis shows this ratio to be increasing increasing at a rate of $\Delta\beta = 0.015$ Pg C/ppm/year, indicating that the ocean accumulation of anthropogenic DIC is increasing at faster rate than atmospheric CO_2 accumulation. This estimate differs from the findings of Müller et al. (2023) of $\Delta\beta < 0$, which suggests a slowdown in the ocean DIC uptake. While the ECCO-Darwin model output has its own biases that could be affecting our estimates, interpolation of observational data such as the method used in Müller et al. (2023) can introduced biases due to spatio-temporal gaps in observations that are skewed towards certain regions and seasons, which tend to be more prevalent in earlier times (e.g., the 1990s). The goal of this study is to add to the existing literature another data point of the estimates of the rates of change of ocean anthropogenic carbon concentrations based on a different dataset such that the overall uncertainty range can be better constrained.

Based on our analysis, the horizontal (depth-integrated, $\widehat{\Delta C^*}$) and vertical (zonally-integrated, $\widetilde{\Delta C^*}$) perspectives taken together reveal a coherent picture of where and how anthropogenic carbon storage has evolved over the past three decades. Across most basins, the large positive $\widetilde{\Delta C^*}$ rates are found in near-surface which is upper 1000 m, particularly in $2002-2022$, suggesting the incorporation of anthropogenic CO_2 into the Mode and Intermediate waters in the Pacific and Indian Oceans (L. D. Talley, 2013). Many parts of the ocean exhibit accelerating increasing rates of anthropogenic carbon concentrations, especially over the $2002-2022$ period. However, we find that ocean anthropogenic carbon accumulation has been slowing down in certain parts of the ocean, specifically the North and Equatorial Pacific and many parts of Southern Ocean. These correspond to the high-nutrient low-chlorophyll parts of the ocean (Coale et al., 1996; Martin, Fitzwater, & Gordon, 1990; Parekh, Follows, & Boyle, 2005) and regions where air-sea CO_2 flux has been identified to drive ocean carbon budget (Carroll et al., 2022). This finding potentially suggests carbon saturation in these parts of the ocean, possibly due to lim-

ited downward transport of oceanic carbon as a result of intensified upper-ocean stratification (Cheng et al., 2025; Sallée et al., 2021).

Another important contribution from this study is the EOF analysis of the interannual variability of the rates of change of C^*, which is possible due to the high and regular temporal resolution of the ECCO-Darwin output compared to observational data. As noted by DeVries et al. (2023), the ECCO-Darwin model has a larger spatial DIC variability compared to other global ocean biogeochemical models and ocean circulation inverse models, which might be due to its ability to more accurately capture climate-driven variability as it strives to provide maximum consistency with observations. While the EOF modes of the variability of the vertically-integrated ΔC^* are not expected to completely agree with climate modes unlike the sea surface temperature that more rapidly responds to changes in the sea surface conditions, we find that over a third of the variability can be predominantly attributed to the Pacific climate modes, namely ENSO, PDO, and NPGO. While ENSO variability has been noted in previous studies (e.g., Carroll et al., 2022; Keppler et al., 2020), the contribution from the other two climate modes has not been considered as thoroughly. We also find that the ENSO climate mode contributes to all of the top four EOF modes, which may be due to its overall impact on the PDO and NPGO modes (Litzow et al., 2020). It is also interesting to note that many regions with larger values of acceleration or deceleration of $\widehat{\Delta C^*}$ rates (Fig. 2) are outside of the equatorial and North Pacific region, i.e., within the subtropical gyres and higher latitudes (the Southern and Arctic Oceans, North/South Atlantic). This suggests that different mechanisms could be contributing to longer term trends and interannual variability of the rate of change of C^*.

It is possible that the timeseries considered here is not long enough to detect climate oscillations with longer periods, such as the Atlantic Multidecadal Oscillation (AMO) (Kerr, 2000). However, we do find the decrease in the North Atlantic uptake of anthropogenic carbon compensated by large increasing rates of C^* in the near-surface Southern Ocean in the 1990s, reminiscent of the AMO mode spatial pattern. We do not find such compensation in the 2000s and 2010s, possibly corresponding to the shift in AMO index from negative to positive around 2000, whether

AMO is due to an internal climate variability or tied to volcanic eruptions such as Mt. Pinatubo in 1991 (Mann, Steinman, Brouillette, & Miller, 2021). Overall, this analysis points to the need for longer and higher temporal resolution timeseries of C^* to examine the effects of these internal climate drivers as they might be partially embedded in the computed decadal rates of change, particularly in low- or mid-latitude regions.

Ultimately, acknowledging the limitations, some of which can be addressed in future studies if higher resolution model outputs become available, this study provides an in-depth analysis of the ocean anthropogenic carbon spatio-temporal variability over the past three decades to enhance our understanding of changes in ocean ability to uptake additional CO_2 from the atmosphere.

Data availability

Data for computed C^* values for each year, analyzed and processed data, and analysis codes are available in the Github repository (`https://github.com/bzemskova/anthropogenic_DIC/`) with DOI: 10.5281/zenodo.17633809

ECCO-Darwin model output is available at the ECCO Data Portal: `http://data.nas.nasa.gov/ecco`.

Global atmospheric carbon dioxide concentrations are available from Lan et al. (2025) through NOAA Global Monitoring Laboratory: `https://gml.noaa.gov/ccgg/trends/global.html`.

The monthly climate indices are available through: AMO `https://psl.noaa.gov/data/timeseries/AMO/`, Atlantic Niño `https://www.cpc.ncep.noaa.gov/products/international/ocean_monitoring/IODMI/ATL3_month.html`, ENSO `https://www.psl.noaa.gov/enso/mei/`, El Niño Modoki `https://www.jamstec.go.jp/aplinfo/sintexf/e/elnmodoki/data.html`, NPGO `https://psl.noaa.gov/data/timeseries/month/DS/NPGO/`, PDO `https://www.ncei.noaa.gov/access/monitoring/pdo/`.

Funding

This research has been supported by the Natural Sciences and Engineering Research Council of Canada (grant numbers: RGPIN-2025-02281 and DGECR-2025-00478) and compute allocation from the Digital Research Alliance of Canada (RRG number 5443).

References

Anderson, L. A., & Sarmiento, J. L. (1994). Redfield ratios of remineralization determined by nutrient data analysis. *Global biogeochemical cycles*, *8*(1), 65–80.

Bronselaer, B., Russell, J. L., Winton, M., Williams, N. L., Key, R. M., Dunne, J. P., ... Sarmiento, J. L. (2020). Importance of wind and meltwater for observed chemical and physical changes in the southern ocean. *Nature Geoscience*, *13*(1), 35–42.

Broullón, D., Pérez, F. F., Velo Lanchas, A., Hoppema, M., Olsen, A., Takahashi, T., ... Kozyr, A. (2020). A global monthly climatology of oceanic total dissolved inorganic carbon: A neural network approach. *Earth System Science Data Discussions*, *2020*, 1–30.

Bushinsky, S. M., Landschützer, P., Rödenbeck, C., Gray, A. R., Baker, D., Mazloff, M. R., ... Sarmiento, J. L. (2019). Reassessing southern ocean air-sea co2 flux estimates with the addition of biogeochemical float observations. *Global biogeochemical cycles*, *33*(11), 1370–1388.

Carroll, D., Menemenlis, D., Adkins, J. F., Bowman, K. W., Brix, H., Dutkiewicz, S., ... Zhang, H. (2020). The ecco-darwin data-assimilative global ocean biogeochemistry model: Estimates of seasonal to multidecadal surface ocean pco and air–sea co flux. *Journal of Advances in Modeling Earth Systems*, *12*(12), e2019MS001888. doi:

Carroll, D., Menemenlis, D., Dutkiewicz, S., Lauderdale, J. M., Adkins, J. F., Bowman, K. W., ... others (2022). Attribution of space-time variability in global-ocean dissolved inorganic carbon. *Global Biogeochemical Cycles*, *36*(3), e2021GB007162. doi:

Carter, B. R., Feely, R. A., Wanninkhof, R., Kouketsu, S., Sonnerup, R. E., Pardo, P. C., ...

others (2019). Pacific anthropogenic carbon between 1991 and 2017. *Global Biogeochemical Cycles*, *33*(5), 597–617.

Cheng, L., Li, G., Long, S.-M., Li, Y., von Schuckmann, K., Trenberth, K. E., ... others (2025). Ocean stratification in a warming climate. *Nature Reviews Earth & Environment*, 1–19.

Chin-Yee, S. (2019). *Climate Change and Human Security: Case Studies Linking Vulnerable Populations to Increased Security Risks in the Face of the Global Climate Challenge* (Strategy Paper). King's College London, EUCERS. Retrieved from `https://discovery.ucl.ac.uk/id/eprint/10084936/7/Chin-Yee_Climatechangeandhumansecurity_VoR.pdf` (Version of record hosted on UCL Discovery)

Clement, D., & Gruber, N. (2018). The emlr(c*) method to determine decadal changes in the global ocean storage of anthropogenic co. *Global Biogeochemical Cycles*, *32*(4), 654–679. doi:

Coale, K. H., Johnson, K. S., Fitzwater, S. E., Gordon, R. M., Tanner, S., Chavez, F. P., ... others (1996). A massive phytoplankton bloom induced by an ecosystem-scale iron fertilization experiment in the equatorial pacific ocean. *Nature*, *383*(6600), 495–501.

Deutsch, C., & Weber, T. (2012). Nutrient ratios as a tracer and driver of ocean biogeochemistry. *Annual review of marine science*, *4*(1), 113–141.

DeVries, T. (2022). The ocean carbon sink. *Annual Review of Environment and Resources*, *46*, 201–230. doi:

DeVries, T., Holzer, M., & Primeau, F. (2019). Decadal trends in the ocean carbon sink. *Proceedings of the National Academy of Sciences*, *116*(24), 11646–11651. doi:

DeVries, T., Yamamoto, K., Wanninkhof, R., Gruber, N., Hauck, J., Müller, J. D., ... Doney, S. C. (2023). Magnitude, trends, and variability of the global ocean carbon sink from 1985 to 2018. *Global Biogeochemical Cycles*, *37*(10), e2023GB007780. doi:

Fay, A., & McKinley, G. (2013). Global trends in surface ocean pco2 from in situ data. *Global Biogeochemical Cycles*, *27*(2), 541–557.

Friedlingstein, P., O'Sullivan, M., Jones, M. W., Andrew, R. M., Gregor, L., Hauck, J., ... Zheng,

B. (2022). Global carbon budget 2022. *Earth System Science Data*, *14*(11), 4811–4900. Retrieved from https://essd.copernicus.org/articles/14/4811/2022/ doi:

Gray, A. R. (2024). The four-dimensional carbon cycle of the southern ocean. *Annual Review of Marine Science*, *16*, 163–190. doi:

Gregor, L., & Gruber, N. (2020). Oceansoda-ethz: a global gridded data set of the surface ocean carbonate system for seasonal to decadal studies of ocean acidification. *Earth System Science Data Discussions*, *2020*, 1–42.

Gruber, N., Clement, D., Carter, B. R., Feely, R. A., van Heuven, S., Hoppema, M., ... Wanninkhof, R. (2019). The oceanic sink for anthropogenic co_2 from 1994 to 2007. *Science*, *363*(6432), 1193–1199. doi:

Gruber, N., & Sarmiento, J. L. (2002). Large-scale biogeochemical-physical interactions in elemental cycles. *The sea*, *12*, 337–399.

Gruber, N., Sarmiento, J. L., & Stocker, T. F. (1996). An improved method for detecting anthropogenic co_2 in the oceans. *Global Biogeochemical Cycles*, *10*(4), 809–837. doi:

Hutchins, D. A., & Tagliabue, A. (2024). Feedbacks between phytoplankton and nutrient cycles in a warming ocean. *Nature Geoscience*, *17*(6), 495–502.

IPCC. (2023). *Sections. in: Climate change 2023: Synthesis report. contribution of working groups i, ii and iii to the sixth assessment report of the intergovernmental panel on climate change.* Geneva, Switzerland: IPCC. (Available at: https://www.ipcc.ch/report/ar6/syr/) doi:

Jackett, D. R., & McDougall, T. J. (1997). A neutral density variable for the world's oceans. *Journal of Physical Oceanography*, *27*(2), 237–263.

JAMSTEC. (2025). *El nino modoki.* https://www.jamstec.go.jp/aplinfo/sintexf/e/elnmodoki/data.html. (Accessed: 2025-11-04)

Keppler, L., Landschützer, P., Gruber, N., Lauvset, S. K., & Stemmler, I. (2020). Seasonal carbon dynamics in the near-global ocean. *Global Biogeochemical Cycles*, *34*(12), e2020GB006571.

Keppler, L., Landschützer, P., Lauvset, S. K., & Gruber, N. (2023). Recent trends and variability

in the oceanic storage of dissolved inorganic carbon. *Global Biogeochemical Cycles*, *37*(5), e2022GB007677.

Kerr, R. A. (2000). A north atlantic climate pacemaker for the centuries. *Science*, *288*(5473), 1984–1985.

Lan, X., Tans, P., & Thoning, K. (2025). *Trends in globally-averaged co2 determined from noaa global monitoring laboratory measurements.* doi:

Landschützer, P., Gruber, N., Haumann, F. A., Rödenbeck, C., Bakker, D. C. E., Van Heuven, S., ... Wanninkhof, R. (2015). The reinvigoration of the southern ocean carbon sink. *Science*, *349*(6253), 1221–1224. doi:

Lauvset, S. K., Lange, N., Tanhua, T., Bittig, H. C., Olsen, A., Kozyr, A., ... others (2022). Glodapv2. 2022: the latest version of the global interior ocean biogeochemical data product. *Earth System Science Data*, *14*(12), 5543–5572.

Liefer, J. D., White, A. E., Finkel, Z. V., Irwin, A. J., Dugenne, M., Inomura, K., ... others (2024). Latitudinal patterns in ocean c: N: P reflect phytoplankton acclimation and macromolecular composition. *Proceedings of the National Academy of Sciences*, *121*(46), e2404460121.

Litzow, M. A., Hunsicker, M. E., Bond, N. A., Burke, B. J., Cunningham, C. J., Gosselin, J. L., ... Zador, S. G. (2020). The changing physical and ecological meanings of north pacific ocean climate indices. *Proceedings of the National Academy of Sciences*, *117*(14), 7665–7671.

Liu, J., Wang, H., Mou, J., Penuelas, J., Delgado-Baquerizo, M., Martiny, A. C., ... others (2025). Global-scale shifts in marine ecological stoichiometry over the past 50 years. *Nature Geoscience*, 1–10.

Locarnini, R. A., Mishonov, A. V., Baranova, O. K., Reagan, J. R., Seidov, D., Zweng, M. M., ... Dukhovskoy, D. (2023). *World ocean atlas 2023, volume 1: Temperature.* NOAA National Centers for Environmental Information. Retrieved from `https://www.ncei.noaa.gov/access/world-ocean-atlas-2023/` (Accessed: 2025-08-13) doi:

Luetz, J. M., & Merson, J. (2020). Climate change and human migration as adaptation: Conceptual and practical challenges and opportunities. In W. Leal Filho, A. M. Azul, L. Brandli, P. Gökcin Özuyar, & T. Wall (Eds.), *Climate action* (pp. 120–132). Cham, Switzerland: Springer International Publishing. (Published online 2019; chapter in Encyclopedia of the UN SDGs) doi:

Mahadevan, A., Lévy, M., & Mémery, L. (2004). Mesoscale variability of sea surface pco2: What does it respond to? *Global Biogeochemical Cycles*, *18*(1).

Mann, M. E., Steinman, B. A., Brouillette, D. J., & Miller, S. K. (2021). Multidecadal climate oscillations during the past millennium driven by volcanic forcing. *Science*, *371*(6533), 1014–1019.

Martin, J. H., Fitzwater, S. E., & Gordon, R. M. (1990). Iron deficiency limits phytoplankton growth in antarctic waters. *Global Biogeochemical Cycles*, *4*(1), 5–12.

Martiny, A. C., Pham, C. T., Primeau, F. W., Vrugt, J. A., Moore, J. K., Levin, S. A., & Lomas, M. W. (2013). Strong latitudinal patterns in the elemental ratios of marine plankton and organic matter. *Nature Geoscience*, *6*(4), 279–283.

Mayot, N., Buitenhuis, E. T., Wright, R. M., Hauck, J., Bakker, D. C. E., & Quéré, C. L. (2024). Constraining the trend in the ocean co_2 sink during 2000–2022. *Nature Communications*, *15*(1), 8429. Retrieved from `https://www.nature.com/articles/s41467-024-52641-7` doi:

McDougall, T. J., & Barker, P. M. (2017). Getting started with teos-10 and the gibbs seawater (gsw) oceanographic toolbox. *SCOR/IAPSO WG*, *127*, 1–28. Retrieved from `https://teos-10.github.io/GSW-Python/density.html`

Messié, M., & Chavez, F. (2011). Global modes of sea surface temperature variability in relation to regional climate indices. *Journal of Climate*, *24*(16), 4314–4331.

Müller, J. D., Gruber, N., Carter, B., Feely, R., Ishii, M., Lange, N., ... Zhu, D. (2023). Decadal trends in the oceanic storage of anthropogenic carbon from 1994 to 2014. *AGU Advances*, *4*(4), e2023AV000875. doi:

NOAA Climate Prediction Center. (2025). *Atlantic 3 index (atl3) by month.* https://www.cpc.ncep.noaa.gov/products/international/ocean_monitoring/IODMI/ATL3_month.html. (Accessed: 2025-11-04)

NOAA National Centers for Environmental Information. (2025). *Pacific decadal oscillation (pdo).* https://www.ncei.noaa.gov/access/monitoring/pdo/. (Accessed: 2025-11-04)

NOAA Physical Sciences Laboratory. (2025a). *Amo (atlantic multidecadal oscillation) index.* https://psl.noaa.gov/data/timeseries/AMO/. (Accessed: 2025-11-04)

NOAA Physical Sciences Laboratory. (2025b). *Multivariate enso index version 2 (mei.v2).* https://www.psl.noaa.gov/enso/mei/. (Accessed: 2025-11-04)

NOAA Physical Sciences Laboratory. (2025c). *North pacific gyre oscillation (npgo).* https://psl.noaa.gov/data/timeseries/month/DS/NPGO/. (Accessed: 2025-11-04)

Parekh, P., Follows, M. J., & Boyle, E. A. (2005). Decoupling of iron and phosphate in the global ocean. *Global Biogeochemical Cycles*, *19*(2).

Pérez, F. F., Mercier, H., Vázquez-Rodríguez, M., Lherminier, P., Velo, A., Pardo, P. C., ... Ríos, A. F. (2013). Atlantic ocean co uptake reduced by weakening of the meridional overturning circulation. *Nature Geoscience*, *6*, 146–152. doi:

Rieger, N., & Levang, S. J. (2024). xeofs: Comprehensive eof analysis in python with xarray. *Journal of Open Source Software*, *9*(93). Retrieved from https://doi.org/10.21105/joss.06060 doi:

Rödenbeck, C., Bakker, D. C., Gruber, N., Iida, Y., Jacobson, A. R., Jones, S., ... others (2015). Data-based estimates of the ocean carbon sink variability–first results of the surface ocean pco 2 mapping intercomparison (socom). *Biogeosciences*, *12*(23), 7251–7278.

Rödenbeck, C., DeVries, T., Hauck, J., Le Quéré, C., & Keeling, R. (2021). Data-based estimates of interannual sea–air co 2 flux variations 1957–2020 and their relation to environmental drivers. *Biogeosciences Discussions*, *2021*, 1–43.

Sabine, C., Key, R., Johnson, K., Millero, F., Poisson, A., Sarmiento, J. L., ... Winn, C. (1999). Anthropogenic co2 inventory of the indian ocean. *Global Biogeochemical Cycles*, *13*(1),

179–198.

Sallée, J.-B., Pellichero, V., Akhoudas, C., Pauthenet, E., Vignes, L., Schmidtko, S., ... Kuusela, M. (2021). Summertime increases in upper-ocean stratification and mixed-layer depth. *Nature*, *591*(7851), 592–598.

Sarmiento, J., & Gruber, N. (2006). Carbon cycle, co2, and climate; the anthropogenic perturbation. *Ocean biogeochemical dynamics*, 399–417.

Schneider, N., & Cornuelle, B. D. (2005). The forcing of the pacific decadal oscillation. *Journal of Climate*, *18*(21), 4355–4373.

Seelen, E. A., Gleich, S. J., Kumler, W., Anderson, H. S., Bian, X., Björkman, K. M., ... others (2025). Nitrogen and phosphorus differentially control marine biomass production and stoichiometry. *Nature Communications*, *16*(1), 5713.

Talley, L., Feely, R., Sloyan, B., Wanninkhof, R., Baringer, M., Bullister, J., ... others (2016). Changes in ocean heat, carbon content, and ventilation: a review of the first decade of go-ship global repeat hydrography. *Annual review of marine science*, *8*, 185–215.

Talley, L. D. (2013). Closure of the global overturning circulation through the indian, pacific, and southern oceans: Schematics and transports. *Oceanography*, *26*(1), 80–97.

Trebilco, R., Fleming, A., Hobday, A. J., Melbourne-Thomas, J., McDonald, J., McCormack, P. C., ... Pecl, G. T. (2022). Warming world, changing ocean: mitigation and adaptation to support resilient marine systems. *Reviews in Fish Biology and Fisheries*, *32*(1), 39–63. Retrieved from `https://doi.org/10.1007/s11160-021-09678-4` (Published online 21 September 2021; issue date March 2022) doi:

United Nations Development Programme (UNDP). (2023). *Mapping of Climate Change Threats in Arab States: Climate Change, Environmental Degradation and Security Impacts* (Technical Report). United Nations Development Programme. Retrieved from `https://www.undp.org/sites/g/files/zskgke326/files/migration/arabstates/Mapping-of-Climate-Change-Threats.pdf` (PDF accessed via UNDP website)

Verdy, A., & Mazloff, M. R. (2017). A data assimilating model for estimating s outhern o cean biogeochemistry. *Journal of Geophysical Research: Oceans*, *122*(9), 6968–6988.

Wanninkhof, R., Doney, S. C., Bullister, J. L., Levine, N. M., Warner, M., & Gruber, N. (2010). Detecting anthropogenic co2 changes in the interior atlantic ocean between 1989 and 2005. *Journal of Geophysical Research: Oceans*, *115*(C11).

Zemskova, V. E., He, T.-L., Wan, Z., & Grisouard, N. (2022). A deep-learning estimate of the decadal trends in the southern ocean carbon storage. *Nature Communications*, *13*, 4056. doi: